

UNIVERSITY OF CALIFORNIA, SAN DIEGO

Seismogeodesy and Rapid Earthquake and Tsunami Source Assessment

A dissertation submitted in partial satisfaction of the
requirements for the degree
Doctor of Philosophy

in

Earth Science

by

Diego Melgar Moctezuma

Committee in charge:

Yehuda Bock, Chair
T. Guy Masters
David T. Sandwell
Peter M. Shearer
Jose I. Restrepo

2014

Copyright
Diego Melgar Moctezuma, 2014
All rights reserved.

The dissertation of Diego Melgar Moctezuma is approved, and it is acceptable in quality and form for publication on microfilm and electronically:

Chair

University of California, San Diego

2014

DEDICATION

To two, the loneliest number since the number one.

EPIGRAPH

*A careful quotation
conveys brilliance.*

—Smarty Pants

TABLE OF CONTENTS

Signature Page	iii
Dedication	iv
Epigraph	v
Table of Contents	vi
List of Figures	viii
List of Tables	ix
Acknowledgements	x
Vita and Publications	xi
Abstract of the Dissertation	xiii
Chapter 1 Introduction	1
1.1 Early Warning and Rapid Response in Natural Hazards	1
1.1.1 More Stuff	1
1.2 Geodesy and Seismology	2
1.3 Earthquake and Tsunami Hazards	2
Chapter 2 Seismogeodesy	3
2.1 Strong Motion Sensing	3
2.2 The role of GPS	9
2.2.1 Displacements in a Local Reference Frame	14
2.3 Seismogeodesy	15
2.3.1 The Kalman Filter Formulation	16
2.3.2 Optimal Smoothing	19
2.3.3 Accelerometer Biases	21
2.4 Proof of Concept	23
2.4.1 Outdoor shake table testing	23
2.5 Application to the M9 Tohoku-oki Earthquake	30
Chapter 3 Rapid Static Modeling	31
3.1 A section	31
Chapter 4 Kinematic Source Inversions	32
4.1 A section	32

Chapter 5	Offshore Data and Tsunami Modeling	33
	5.1 A section	33
Chapter 6	Conclusions and Future Outlook	34
	6.1 A section	34

LIST OF FIGURES

Figure 1.1: A figure of Vonnegut.	1
Figure 2.1: Effect of numerical integration on a strong motion recording. . .	5
Figure 2.2: Some simple baseline corrections.	7
Figure 2.3: 1 Hz GPS time series at Parkfield	13
Figure 2.4: 2006 shake table experiment configuration	24
Figure 2.5: 2006 shake table experiment Kalman filtered waveforms	29

LIST OF TABLES

Table 2.1:	A summary of Kalman filtering and smoothing equations	20
Table 2.2:	2006 shake table test results	26

ACKNOWLEDGEMENTS

Thanks to whoever deserves credit for Blacks Beach, Porters Pub, and every coffee shop in San Diego.

Thanks also to hottubs.

VITA

2009	B. Eng. in Geophysics <i>cum laude</i> , Universidad Nacional Autonoma de Mexico
2010	M. Sc in Earth Science University of California, San Diego
2014	Ph. D. in Earth Science, University of California, San Diego

PUBLICATIONS

Crowell, B.W., **Melgar, D.**, Bock, Y., Haase, J.S, and Geng, J., “Earthquake Magnitude Scaling using Seismogeodetic Data”, *Geophys. Res. Lett*, 40(23), 2013.

Melgar, D. and Bock, Y. “Near-Field Tsunami Models with Rapid Earthquake Source Inversions from Land- and Ocean-Based Observations: The Potential for Forecast and Warning”, *J. Geophys. Res.*, 118(11), 2013.

Geng, J., **Melgar, D.**, Bock, Y., Pantoli, E., and Restrepo, J.I., “Recovering coseismic point ground tilts from collocated high-rate GPS and accelerometers”, *Geophys. Res. Lett*, 40(19), 2013.

Melgar, D., Pantoli, E., Bock, Y., and Restrepo, J.I., “Displacement Acquisition for the NEESR:BNCS Building Shaketable Test via GPS Sensors”, *Network for Earthquake Engineering Simulation (distributor)*, DOI:10.4231/D3V97ZR5H, 2013.

Melgar, D., Crowell, B.W., Bock, Y., and Haase, J.S, “Rapid modeling of the 2011 Mw 9.0 Tohoku-oki earthquake with seismogeodesy”, *Geophys. Res. Lett*, 40(12), 2013.

Geng, J., Bock, Y., **Melgar, D.**, Crowell, B.W., and Haase, J.S, “A new seismogeodetic approach applied to GPS and accelerometer observations of the 2012 Brawley seismic swarm: Implications for earthquake early warning”, *Geochem. Geophys. Geosyst*, 14(7), 2013.

Melgar, D., Bock, Y., Sanchez, D., and Crowell, B.W., “On Robust and Reliable Automated Baseline Corrections for Strong Motion Seismology”, *J. Geophys. Res.*, 118(3), 2013.

Perez-Campos, X., **Melgar, D.**, Singh, S.K., Cruz-Atienza, V., Iglesias, A., and Hjorleifsdottir, V., “Determination of tsunamigenic potential of a scenario earthquake in the Guerrero seismic gap along the Mexican subduction zone”, *Seism. Res. Lett*, 84(3), 2013.

Crowell, B.W., Bock, Y., and **Melgar, D.**, “Real-time inversion of GPS data for finite fault modeling and rapid hazard assessment”, *Geophys. Res. Lett.*, 39(9), 2012.

Singh, S.K., Perez-Campos, X., Iglesias, A., **Melgar, D.**, “A Method for Rapid Estimation of Moment Magnitude for Early Tsunami Warning Based on Coastal GPS Networks”, *Seism. Res. Lett.*, 83(3), 2012.

Melgar, D., Bock, Y., and Crowell, B.W., , “Real-Time Centroid Moment Tensor Determination for Large Earthquakes from Local and Regional Displacement Records”, *Geophys. J. Int.*, 188(2), 2012.

Bock, Y., **Melgar, D.**, and Crowell, B.W., “Real-Time Strong-Motion Broadband Displacements from Collocated GPS and Accelerometers”, *Bull. Seism. Soc. Am.*, 101(6), 2011.

Melgar, D. and Perez-Campos, X., “Imaging the Moho and Subducted Oceanic Crust at the Isthmus of Tehuantepec, Mexico, from Receiver Functions”, *Pure Appl. Geophysics*, 168, 2010.

ABSTRACT OF THE DISSERTATION

Seismogeodesy and Rapid Earthquake and Tsunami Source Assessment

by

Diego Melgar Moctezuma

Doctor of Philosophy in Earth Science

University of California, San Diego, 2014

Yehuda Bock, Chair

This dissertation will be abstract.

Chapter 1

Introduction

This is only a test.

1.1 Early Warning and Rapid Response in Natural Hazards

Lorem ipsum dolor sit amet, consectetur adipiscing elit. Nulla odio sem, bibendum ut, aliquam ac, facilisis id, tellus. Nam posuere pede sit amet ipsum. Etiam dolor. In sodales eros quis pede. Quisque sed nulla et ligula vulputate lacinia. In venenatis, ligula id semper feugiat, ligula odio adipiscing libero, eget mollis nunc erat id orci. Nullam ante dolor, rutrum eget, vestibulum euismod, pulvinar at, nibh. In sapien. Quisque ut arcu. Suspendisse potenti. Cras consequat cursus nulla.

1.1.1 More Stuff

Blah

*

Figure 1.1: A figure of Vonnegut.

1.2 Geodesy and Seismology

1.3 Earthquake and Tsunami Hazards

Chapter 2

Seismogeodesy

A brief summary of what is discussed in this chapter

2.1 Strong Motion Sensing

The range of motions produced by the seismic source is broad both in frequency and dynamic range. It is well known that no one sensor can capture all signals of interest to seismology and earthquake engineering (*Havskov and Alguacil, 2006*). Seismologists typically rely on seismometers, whose response is related to velocity of the ground, for measurement of small amplitude signals (weak motion), but for large amplitude signals these sensitive instruments saturate or clip. In this case, strong motion sensors, whose response is related to the acceleration of the ground and have lower gains, are preferred. Modern observatory grade accelerometers rely on the force feedback principle and can measure motions as small as 1 nm at 1 Hz and 100 nm at 0.1 Hz and accelerations of up to 4g. Furthermore their frequency response is flat from) (often called the DC-level) to 50-200 Hz (*Havskov and Alguacil, 2006*).

Thus, in principle there should be no difficulty in integrating a strong motion record to velocity and displacement. This is not the case; in practice the simple integration of an accelerogram produces unphysical velocity and displacement waveforms that grow unbounded as time progresses. Computation of broadband displacements from strong motion recordings is a thoroughly studied procedure

that is fraught with many known problems and has no known single solution. By “broadband displacement” it is meant a strong motion displacement waveform that captures both transient phenomena (waves) and permanent or static deformation, i.e. a recording reliable from DC to the Nyquist frequency.

The problems associated with the double integration of accelerometer recordings have been comprehensively studied and many sources of error have been suggested: numerical error in the integration procedure, mechanical hysteresis, cross-axis sensitivity and unresolved rotational motions (*Graizer, 1979; Iwan et al., 1985; Boore, 1999, 2001; Boore et al., 2002; Smyth and Wu, 2007*). It is generally assumed that small offsets are introduced in the acceleration time series; upon integration these baseline offsets produce the linear and quadratic trends observed in the velocity and displacement time series, respectively. Many possible sources have been invoked as the source of these offsets with unresolved rotational motion increasingly considered the main error (*Graizer, 2006; Pillet and Virieux, 2007*). Motion is described by six degrees of freedom, three translations and three rotations. Accelerometers are incapable of discerning between rotational and translational motions, thus, rotational motions are recorded as spurious translations. Effectively, this results in a change of the baseline of the accelerometer, even if by a small amount, leading to unphysical drifts in the singly integrated velocity waveforms and doubly integrated displacement waveforms (Figure 2.1).

Many correction schemes, collectively known as baseline corrections, have been proposed over time to deal with this problem. Rotational motions become more prevalent close to the source and at long periods. In particular *Trifunac and Todorovska (2001)* have shown that rotational motions have significant contributions to radiated spectra and can sometimes be the predominant source of seismic energy, particularly at very long periods and for very large earthquakes.

The simplest baseline correction scheme is a high-pass filter (*Boore and Bommer, 2005*). This leads to accurate recovery of the mid to high frequency part of the displacement record but suppresses completely long period information such as the static offset (Figure 2.2). To ameliorate this, a number of more elaborate correction schemes exist (*Boore and Bommer, 2005*) that rely on function fitting to

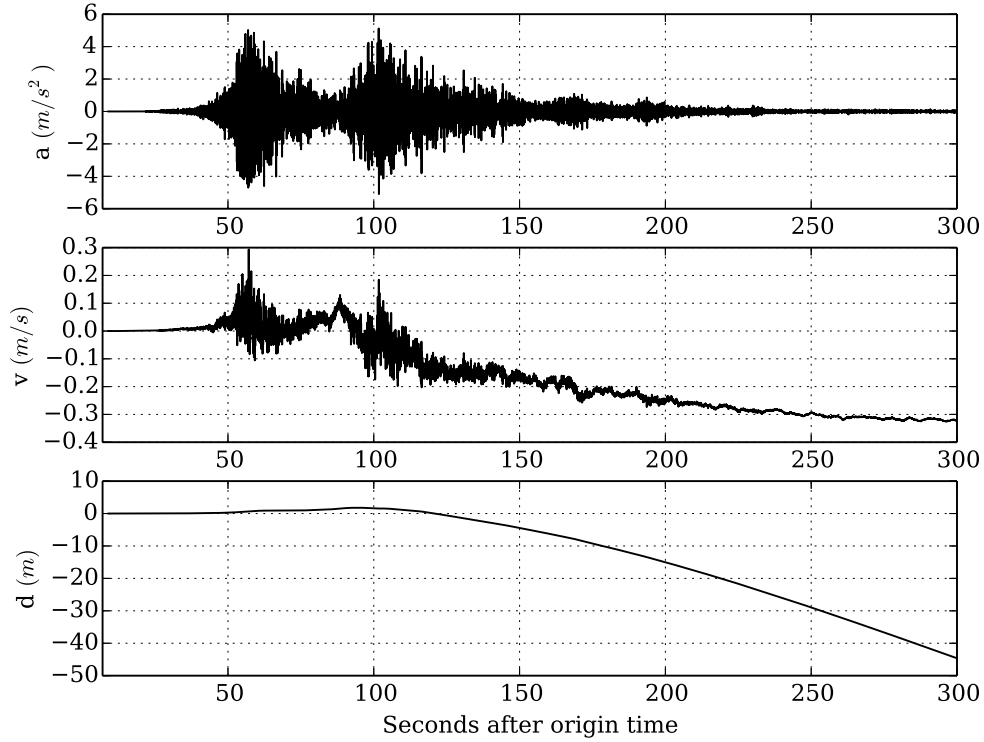


Figure 2.1: Effect of numerical integration on a strong motion accelerogram. This example is for the east component of motion at station IWT009 192 km from the centroid of the 2011 M9 Tohoku-oki earthquake. Note the unphysical drifts in both the velocity and displacement time series.

the singly integrated velocity time series. The most reliable scheme that routinely produces plausible displacement waveforms (which include a measure of the static offset) is described in *Boore* (1999, 2001) and is a modification of the scheme proposed by *Iwan et al.* (1985) and henceforth referred to as the Boore-Iwan or BI correction scheme. In this method a piece-wise linear function is fit to the uncorrected velocity time series, the slope of each straight line segment represents an acceleration step which is then subtracted from the original acceleration data. This baseline corrected acceleration record is subsequently integrated to velocity and displacement. If the intervals for fitting the linear functions to the velocity data are selected appropriately this algorithm will produce waveforms that look plausible. They will contain both permanent and transient motions. The difficulty

then lies in determining what these appropriate time intervals are from the data themselves. As discussed by *Boore* (1999, 2001) this is an ambiguous process. To diminish this uncertainty, subsequent research has focused on determining plausible times for the fits and then grid searching for waveforms that most resembles a ramp or step function (*Wu and Wu*, 2007; *Chao et al.*, 2010; *Wang et al.*, 2011).

This is better understood through an example. Consider the time series of Figure 2.1. The traditional BI correction procedure starts by removing the pre-event mean or baseline, this is called the zeroth order corrected waveform. Then for some analyst determined initial correction time t_i and final correction time t_f , two baselines or acceleration steps can be computed from the drift in the velocity data and subsequently removed. Underlying this process is the assumption that from time t_i to some intermediate time t_1 (determined by the analyst) a baseline offset due to strong shaking is introduced into the time series and subsequently from this intermediate time t_1 to the final correction time t_f a *permanent* baseline offset is introduced into the data. Thus, the first acceleration step is determined by a least squares straight line fit to the velocity data between times t_1 and t_f such that

$$v_f(t) = v_0 + a_f(t) ; t \in (t_1, t_f) , \quad (2.1)$$

where the regression parameters are v_0 and the acceleration step a_f . Subsequently, another straight line is fit from t_i to t_1 with the constraint that velocity be zero at the start of the record and that the final velocity averages to zero. These constraints are satisfied if (*Boore*, 1999)

$$a_m = \frac{v_f(t_1)}{t_1 - t_i} . \quad (2.2)$$

Then, the acceleration baseline, a_m , is subtracted from the uncorrected record from times t_i to t_1 and the baseline offset, a_f , is subtracted from the zeroth order corrected record for times t_1 to t_f . The record is then integrated to velocity and displacement. This scheme produces waveforms that look plausible; they contain both transient and permanent motions. However an ambiguity lies in the selection of times t_i and t_1 . As has been amply discussed by *Boore* (1999, 2001), this ambiguity is not easily resolved without external information and each investigator

relies on subjective judgment to ascertain what looks best. Figure 2.2 illustrates such an example where the same waveform has been baseline corrected for several values of t_1 while holding t_i fixed at the P wave arrival time with results that vary wildly. If the waveform is complex, as in this example, which has two distinct pulses of very strong shaking, then more baselines might need to be subtracted. However, if there is already ample ambiguity in the simple determination of the two baselines a_m and a_f , the problem is exacerbated with the introduction of more baselines.

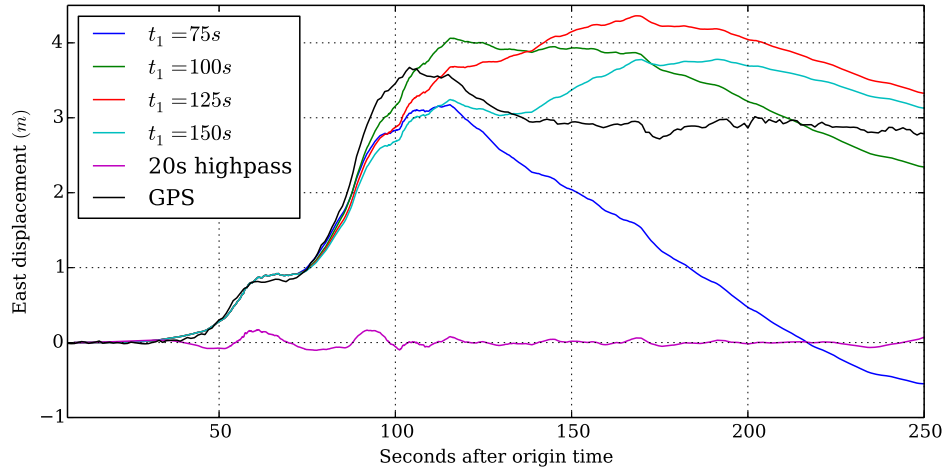


Figure 2.2: Baseline corrections using the BI algorithm for the east component of motion at station IWT009 192 km from the centroid of the 2011 M9 Tohoku-oki earthquake using different values of the correction parameter t_1 . Also shown is the result of a 20s high pass filter corrected waveform and the GPS displacements recorded at the same site

The correction times t_i and t_1 can and do vary for each station-event pair and even for different channels at the same station during the same event. Practically this means that analysis of broadband displacements from baseline-corrected accelerometer records is inherently ambiguous and complicated for real-time seismological applications or across large networks both for real-time and post-processing purposes.

Research into automated baseline correction from accelerometer data alone has focused on variations of the BI scheme. *Wu and Wu (2007)* proposed a variant

in which the times for each linear segment of the baseline correction are determined by a grid search such that the resulting time series best matches a ramp function. *Chao et al.* (2010) elaborated on the formulation of *Wu and Wu* (2007) by adding an extra restriction that the times be selected after certain threshold values of acceleration energy have been accrued. Both studies compare their results to static offsets determined from GPS and find that their estimates are somewhat similar. They still maintain some significant differences though, and no analysis on the adequacy of the remaining part of the waveform is performed. It is implicitly assumed that if the static field is well fit then the rest of the waveform will be reliable as well.

An important advance in automatic baseline correction is presented in *Wang et al.* (2011) who present another variation of the BI bilinear scheme that performs better than those discussed thus far. They develop some simple rules for determination of the interval of possible correction times based on analysis of the uncorrected acceleration and displacement waveforms. From an analysis of the time at which the peak ground acceleration (PGA) occurs and the time of last zero crossing in the uncorrected displacement they determine bounds for the grid search of baseline correction times. They then perform the grid search among these possible correction times and fit, via a non-linear regression, a step function to all possible waveforms. An optimum correction (the one that best fits this step function) is then selected. Unlike previous studies they compare their results not only to measured static offsets but to observed 1 Hz GPS data; they do this for a single station. They find for that one station an error of $\sim 20\%$ in the static field estimation but a very good agreement between the corrected displacement and the GPS for the first 200s of the waveform.

In a follow up study *Wang et al.* (2013) apply their methodology to accelerometer records for the 2011 Mw 9.0 Tohoku-oki earthquake. They obtain reasonable estimates of the static field for many stations in the KiK-net network in Japan but also find numerous outliers. They then develop a simplified scheme to screen the outliers by excluding coseismic offsets that deviate more than 15 from the predictions of a static slip inversion. Furthermore, they compare their

automatic corrections for selected borehole sensors in the KiK-net network with nearby high-rate GPS stations with mixed results. They find that while parts of the waveforms might be a good match, the static estimates can be in error by a significant amount. To ameliorate this they then propose to use the static field from nearby GPS stations as a constraint in the correction procedure. From the pool of all candidate baseline corrections they select the one that fits a step function of amplitude given by the static field. In a follow up study *Tu et al.* (2014) showed that substantial improvement was possible if corrections were correlated between neighboring stations of a dense network. It is noteworthy that *Wang et al.* (2013) and *Tu et al.* (2014) and do not provide baseline corrected solutions for the sister strong motion network K-net. They readily acknowledge that K-net stations, which generally have less favorable site responses (*Tsuda et al.*, 2006), are not well modeled by this automatic approach. This will be important later on in this chapter when it is shown that K-net data can be corrected as well as KiK-net data. In general while these algorithms have demonstrated incremental improvements to the original BI correction scheme they are far from being routinely applicable, objective or automatable.

The availability of suitable correction algorithms for strong motion waveforms that can produce broadband displacements is of broad interest especially for source analysis and hazards assessment. There has been ample interest in recent years to access to such real-time broadband displacements. Recall that it is the long periods of the seismic spectrum down to the static offset that provide the most obvious demarcation between large events. Static offsets and long period radiation can be used to rapidly compute moment tensors, source dimensions, static and kinematic source models and tsunami models. Indeed in Chapters 3,4 and 5 we will show how broadband strong motion waveforms facilitate such computations.

2.2 The role of GPS

An alternative to baseline corrections of strong motion data is to measure displacements directly using the Global Positioning System (GPS). There are two

basic approaches to precise GPS data analysis: network positioning and precise point positioning. In both approaches stations positions are estimated with respect to a global Cartesian terrestrial reference system. This system is realized by the published coordinates and velocities of hundreds of global geodetic stations in the International Terrestrial Reference Frame (ITRF). Precise GPS satellite orbital products distributed by the International GNSS Service (IGS) are tied to this underlying reference frame, and without loss of generality, are assumed to be fixed in the GPS data analysis.

In network positioning, data from a network of stations are analyzed simultaneously to estimate station positions and integer-cycle phase ambiguities (*Dong and Bock, 1989; Blewitt, 1989*), and other parameters such as zenith troposphere delays. Analyzing the data as a network, results in the effective cancellation of GPS receiver clock and satellite clock errors, which are common to multiple satellite and stations, respectively. Precise point positioning (*Zumberge et al., 1997*) relies on fixed satellite orbits, as well as satellite clock parameters also available through the IGS and/or its different analysis centers. These parameters are held fixed in the process of estimating ITRF positions of individual CGPS stations, phase ambiguities, zenith troposphere delays and station clock parameters.

Network positioning and precise point positioning approaches can be considered equivalent, in terms of the underlying physics. However, to achieve geodetic quality positions (mm- to cm-level), it is essential to resolve integer-cycle phase ambiguities to their correct integer values (*Blewitt, 1989; Dong and Bock, 1989*). This is straightforward for batch post-processing, which includes the simultaneous analysis of multiple GPS data records, usually sampled at rates of 15-30 s, to derive a single station position over the entire sampled interval. It is the source of the typical 24-hour GPS position time series used to study permanent deformation, including long-term tectonic motion, as well as coseismic, postseismic and other transient deformation. Batch post-processing plays a role in seismological applications by providing highly-accurate, true-of-date ITRF station positions with respect to which displacement waveforms can be estimated during an event. There are several analysis groups that are producing 24-hour position time series on an

operational basis.

Of primary importance in seismological applications is the estimation of cm-level or better displacements at the GPS receiver sampling rate, typically 1 Hz. Since the first pioneering efforts over a decade ago (*Nikolaidis et al.*, 2001; *Larson et al.*, 2003; *Bock et al.*, 2004; *Miyazaki et al.*, 2004) post-processed single-epoch network positioning with resolution of integer-cycle phase ambiguities is now routinely applied to seismology. However, a general real-time solution is still elusive, and analysis of multiple data epochs is usually required to resolve integer-cycle phase ambiguities and estimate single-epoch positions.

In the network positioning approach typically, and for computational efficiency, the larger network is divided into multiple subnetworks with a 2-station overlap between adjacent subnetworks, and positions are estimated relative to the true-of-date ITRF coordinates of an arbitrary station within each subnetwork. Then, a network adjustment is performed to estimate coordinates for all stations with respect to the true-of-date ITRF coordinates of one or more stations outside the zone of deformation (*Crowell et al.*, 2009) easily providing centimeter level resolution.

Precise point positioning has been limited in GPS seismology, in particular for real-time applications, because of unresolved integer-cycle phase ambiguities and slow convergence rates and re-convergence rates when loss of lock on the satellite signals occurs. JPL's Global Differential GPS (GDGPS) System employs a large global ground network of real-time reference receivers and real-time data processing software, which allows a single GPS receiver to be point positioned with 10-20 cm accuracy anywhere in the world. This level of accuracy is considered useful for global tsunami warning generated by great earthquakes. A relatively new area of geodetic research is rapid integer cycle ambiguity resolution in precise point positioning (PPP-AR), without the need for specific reference stations. Besides fixed satellite orbits and clocks, and estimation of positions, receiver clocks and tropospheric delays of the GPS signals, it also requires prediction of ionospheric delays. Recent results have been encouraging in that reliable ambiguity resolution and cm-level positioning accuracies have been achieved with only a few epochs of

1 Hz GPS data for re-convergence. *Geng* (2010). It has seance been shown with a study of modestly sized earthquakes (M5) during the 2013 Brawley swarm (*Geng et al.*, 2013a) and shake table tests (*Geng et al.*, 2013b) that the PPP-AR method is evolving to a state were it can be considered viable technology for real-time and rapid position calculations with cm-level precision.

It is important for the reader to understand the benefits and shortcomings of these two competing technologies. The network adjusted positions have routinely provided cm-level waveforms (*Crowell et al.*, 2009). However, they require that the base station for the adjustment be located outside the zone of deformation and that it not move during the event. Evidently this requires a large network with good connectivity and some strategy fir detecting motions of the reference station and a fall back plan to another station hat has not moved during the event. Furthermore this approach requires to convert the baselines between stations in subnetworks or triangles into absolute motions. This is essentially a solution to an inverse problem at each epoch. While this is not numerically troublesome as the number of stations increases and as sampling rates increase as well the numerical load will grow. In contrast the PPP-AR approach does not require such a reference station (although it does rely on a sparse continental network for computation of certain positioning parameters, (*Geng et al.*, 2013a) and is thus, in principle, more desirable. However ambiguity resolution might fail and convergence periods, at least initially can still be long. Throughout this dissertation data from both network adjusted and PPP-AR positions will be employed. It's not the aim of this work to assess the suitability of one technique over the other although some general recommendations will be given in the conclusions. Hence for the purpose of the research discussed both approaches will be considered equal.

In general GPS seems desirable over traditional seismometry for displacement computations because it is not besieged by baseline offsets because it is not an inertial sensor. This has the practical effect of making GPS a very good long and ultra-long period sensor. It can easily measure signals with very long periods, such as plate tectonic motions and post-seismic relaxation. Consider Figure 2.3, note how the time series shows the (relative) long term plate rate as a linear trend,

the coseismic offset from the September 28, 2004 Mw=6.0 Parkfield earthquake and the postseismic relaxation as well as some shaking during the earthquake. GPS captures key components of the seismic cycle.

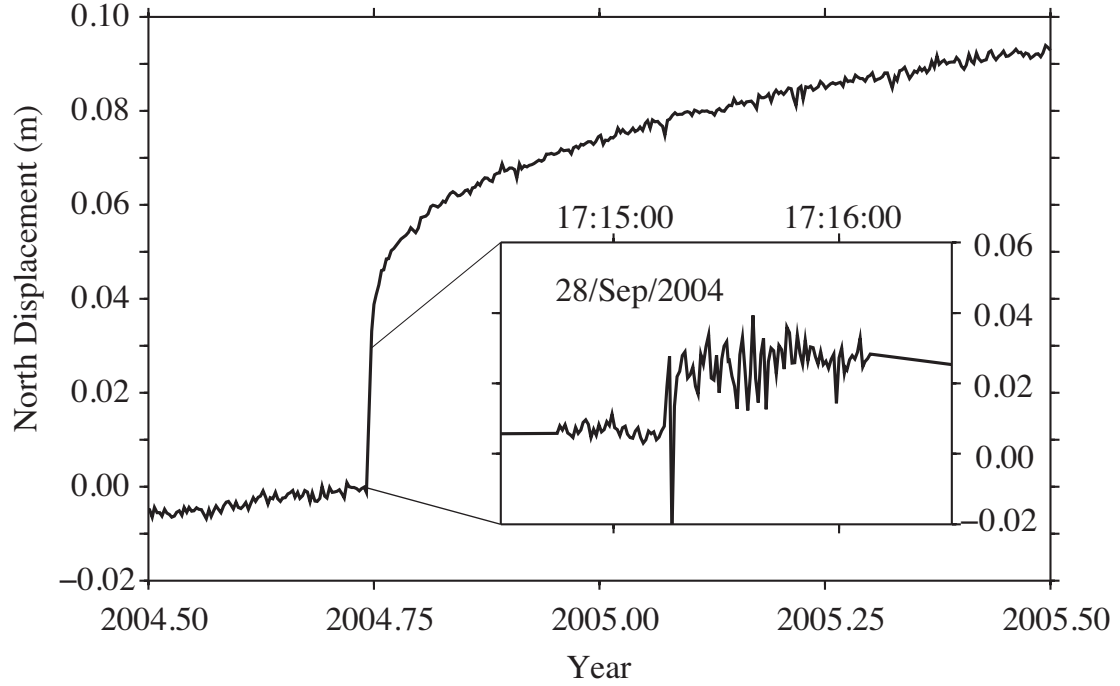


Figure 2.3: Typical 1 Hz GPS raw time series at station LAND (35.8997 N, 120.4731 W) in the Parkfield area over a one-year period. Shown is the north component, in this case relative to station CRBT (N 35.7916, 120.7507 W) whose coordinates were fixed in the GPS analysis. Note how the time series shows the (relative) long term plate rate as a linear trend, the coseismic offset from the September 28, 2004 Mw=6.0 Parkfield earthquake and the postseismic relaxation. In the inset, 2 minutes of data are shown where as opposed to the daily solutions time series we can also observe the (relative) dynamic shaking during the earthquake.

However noise levels in high rate real-time GPS (rtGPS) displacements (*Genrich and Bock, 2006*) far exceed those of observatory grade accelerometers. Furthermore GPS data is far more verbose than seismic data. While a traditional telemetry packet for a seismic sensor at a given epoch might include three single or double precision floating point numbers corresponding to the three components of motion and a UTC time string, the GPS message includes observables to every visible satellite. This has limited the sampling rates of rtGPS to around 1-5Hz

even though $10\text{-}50\text{Hz}$ is achievable (*Genrich and Bock, 2006*). These slow sampling rates can introduce significant aliasing in GPS positions (*Smalley, 2009*). In spite of these limitations, it will be shown that without GPS positions it is exceedingly difficult to recover the long period component of ground motions and that GPS plays an important role in modern strong motion seismology.

2.2.1 Displacements in a Local Reference Frame

Finally, it must be noted GPS positions are typically computed in a global reference frame (i.e. ITRF) in what is known as Earth centered Earth fixed coordinates. This is a right handed system where the three cartesian axes have an origin at the geodetic center of the planet, one axis points towards the geodetic pole and two towards the equator. Without loss of generality or consideration for the particular GPS analysis technique used, or whether or not performed in real time or post processing, we assume that displacement waveforms are available for a geophysical event (e.g., earthquake) for one of more continuous GPS (CGPS) stations with centimeter-level or better single-epoch precision at, for example, the typical 1 Hz sampling rate of current real-time geodetic networks. Consider that we know the precise coordinates (x_0, y_0, z_0) of a CGPS station in a global Cartesian reference frame just prior to an earthquake, at time t_0 . The prior coordinates represent “true-of-date” values. The station is then subjected to a combination of dynamic and static displacements. The subsequent coordinates of the station are denoted by (x_i, y_i, z_i) , where i denotes the i -th epoch after the event. The displacement at the i -th epoch can be simply computed as $(x_i - x_0, y_i - y_0, z_i - z_0)$. In order to compare the geodetic displacements to displacements derived from a single integration of a seismometer or double integration of an accelerometer, we need to transform the displacements from a (right-handed) global Cartesian frame (x, y, z) into a (left-handed) local North, East, Up frame (N, E, U) by the following transformation

$$\begin{pmatrix} \Delta N_i \\ \Delta E_i \\ \Delta U_i \end{pmatrix} = \begin{pmatrix} 1 & 0 & 0 \\ 0 & 1 & 0 \\ 0 & 0 & 1 \end{pmatrix} \mathbf{R}_2\left(\frac{3\pi}{2} - \phi\right) \mathbf{R}_3(\lambda) \begin{pmatrix} x_i - x_0 \\ y_i - y_0 \\ z_i - z_0 \end{pmatrix} ; \quad (2.3)$$

where \mathbf{R}_2 and \mathbf{R}_3 are rotation matrices around the y and z axes, respectively, and (ϕ, λ) is the geodetic latitude and longitude of the station. The geodetic displacements in the (N, E, U) frame can then be compared directly to local displacements derived through single integration of seismometer data or double integration of accelerometer data. Thus, Equation 2.3 simplifies to:

$$\begin{pmatrix} \Delta N_i \\ \Delta E_i \\ \Delta U_i \end{pmatrix} = \begin{pmatrix} -\sin \phi \cos \lambda & \sin \phi \sin \lambda & \cos \phi \\ -\sin \lambda & \cos \lambda & 0 \\ \cos \phi \cos \lambda & \cos \phi \sin \lambda & \sin \phi \end{pmatrix} \begin{pmatrix} x_i - x_0 \\ y_i - y_0 \\ z_i - z_0 \end{pmatrix}. \quad (2.4)$$

2.3 Seismogeodesy

As discussed in the previous section both traditional seismometry and GPS have advantages and disadvantages when it comes to sensing strong ground motions. Most importantly GPS and strong motion networks are complementary in the sense that ones weakness can be complemented by anthers strength. In particular GPS has slow sampling rates while accelerometers have fast sampling rates; in turn accelerometers suffer from problems at long periods while GPS excels in this frequency band. Throughout this section we will show that the combination of these two sensor types provides an accurate representation of ground motion at all frequencies of interest to seismology.

We define the term *seismogeodesy* as the optimal combination of geodetic and seismic data. This has been attempted before, *Nikolaidis et al.* (2001) showed that accelerometer data could be manipulated to fit 30 s sampled data recorded during the 1999 M7.1 Hector Mine earthquake. *Emore et al.* (2007) used 1 Hz GPS data and 100 Hz strong motion data recorded during the M8.3 Tokachi-oki event in 2003 to compute *seismogeodetic* displacements. He did so by solving an inverse problem for the baseline offsets in the accelerometer record. In his approach the model parameters were the baseline offsets that when subtracted from the accelerometer record would best fit, after double integration, the GPS record. This approach yielded good results, however the setup of the inverse problem is cumbersome, int he following section we will show an alternate approach. Using a Kalman filter, we optimally combine raw very-high-rate (e.g., 100-200 Hz) accel-

erations with high-rate (e.g., 1-10 Hz) displacements derived from collocated GPS receivers to estimate very-high-rate displacements. This approach is suitable for dense networks and real-time processing required by early warning systems and rapid earthquake response.

2.3.1 The Kalman Filter Formulation

In the theory of control and estimation the problem of extracting, separating or detecting a random signal in the presence of noise is known as the Wiener problem. Kalman filters are a solution to this problem using the state-space representation of dynamical systems (*Kalman, 1960*). A dynamical system can be characterized by its state. The state can be understood as all the information about the past behavior of the system necessary to predict its future behavior. The dynamics of the system are then described by state transitions. If the goal is to track the motion of a particle subject to Newton's laws of motion and some stochastic noise then a simple continuous difference equation can be setup (*Lewis et al., 2008*). The system states will be the position d and velocity v of the particle, such that

$$\frac{d}{dt} \begin{pmatrix} d(t) \\ v(t) \end{pmatrix} = \frac{d}{dt} \mathbf{x}(t) = \mathbf{A}(t)\mathbf{x}(t) + \mathbf{B}(t)u(t) + \epsilon(t) , \quad (2.5)$$

where

$$\mathbf{x}(t) = \begin{pmatrix} d(t) \\ v(t) \end{pmatrix} ; \mathbf{A} = \begin{pmatrix} 0 & 1 \\ 0 & 0 \end{pmatrix} ; \mathbf{B} = \begin{pmatrix} 0 \\ 1 \end{pmatrix} ; u = a ; \epsilon = \begin{pmatrix} 0 \\ \epsilon_a \end{pmatrix} , \quad (2.6)$$

where ϵ_a is the noise in the acceleration of the particle at any given time step. For the traditional Kalman filter Gaussian noise is assumed and the noise vector will be distributed like $\epsilon \sim (0, \mathbf{Q})$ where the covariance \mathbf{Q} depends just on the acceleration noise σ_a

$$\mathbf{Q} = \begin{pmatrix} 0 & 0 \\ 0 & \sigma_a \end{pmatrix} . \quad (2.7)$$

We can combine Equations 2.5 and 2.6 to verify the system

$$\frac{d}{dt} \begin{pmatrix} d(t) \\ v(t) \end{pmatrix} = \begin{pmatrix} \dot{d} \\ \dot{v} \end{pmatrix} = \begin{pmatrix} v \\ a \end{pmatrix} . \quad (2.8)$$

This definition for such a simple system seems tautological, however verifying the setup of the continuous difference equation will be important later on when we build extra complexities into the filter. Next we must discretize this continuous representation of the system such that

$$\mathbf{x}_{k+1} = \mathbf{A}^s \mathbf{x}_k + \mathbf{B}^s a_k + \epsilon_k , \quad (2.9)$$

where the superscript s denotes the discretized or sampled version of the state transition matrices and the subscript k denotes a discrete time step. The discretized noise vector is Gaussian and distributed like $\epsilon_k \sim (0, \mathbf{Q}^s)$. If we sample the continuous system at the sampling rate τ_a of the acceleration steps affecting the system then the state transition matrices are altered. From the canonical solution to Equation 2.5 *Lewis et al.* (2008) show that the state transition matrices are obtained by a MacLaurin expansion of the integral forms such that

$$\mathbf{A}^s = \mathbf{I} + \mathbf{A}\tau_a + \frac{\mathbf{A}^2\tau_a^2}{2} = \begin{pmatrix} 1 & \tau_a \\ 0 & 1 \end{pmatrix} , \quad (2.10)$$

$$\mathbf{B}^s = \mathbf{B}\tau_a + \frac{\mathbf{A}\mathbf{B}\tau_a^2}{2} = \begin{pmatrix} \tau_a^2/2 \\ \tau_a \end{pmatrix} , \quad (2.11)$$

$$\mathbf{Q}^s = \mathbf{Q}\tau_a + \frac{1}{2}(\mathbf{A}\mathbf{Q} + \mathbf{Q}\mathbf{A}^T)\tau_a^2 + \frac{1}{3}\mathbf{A}\mathbf{Q}\mathbf{A}^T\tau_a^3 = \begin{pmatrix} \sigma_a\tau_a^3/3 & \sigma_a\tau_a^2/2 \\ \sigma_a\tau_a^2/2 & \sigma_a\tau_a \end{pmatrix} . \quad (2.12)$$

This completes the description of the linear system. The Kalman filter is the sequence of mathematical manipulations necessary to estimate the state \mathbf{x}_k of the system at each time step k given the noisy accelerations affecting the system. The formulation of the filter begins by introducing a measurement of the system states, that, unlike the transition matrices, are not altered by the discretization process (*Lewis et al.*, 2008). Assuming we are measuring only displacement this can be written like

$$z_k = d_k^{obs} = \mathbf{H}^s \mathbf{x}_k + \eta_d , \quad (2.13)$$

where d_k^{obs} is the GPS measurement of displacement at epoch k with white Gaussian noise such that $\eta_d \sim (0, R^s)$. Sampling at the rate of the GPS, τ_d the discretized matrices are simply:

$$\mathbf{H}^s = \mathbf{H} = \begin{pmatrix} 1 & 0 & 0 \end{pmatrix} , \quad (2.14)$$

$$R^s = \sigma_d / \tau_d . \quad (2.15)$$

First we estimate the system state covariance \mathbf{P} . After initializing the system states and covariance to \mathbf{x}_0 and \mathbf{P}_0 (usually zero or the identity) *Kalman* (1960) showed, and subsequent workers proved (see *Lewis et al.* (2008)) that an unbiased minimum error estimate could be obtained by computing the *a priori* covariance as

$$\mathbf{P}_{k+1}^- = \mathbf{A}_k \mathbf{P}_k \mathbf{A}_k^T + \mathbf{Q}_k , \quad (2.16)$$

and the a priori state estimate as

$$\hat{\mathbf{x}}_{k+1}^- = \mathbf{A}_k \hat{\mathbf{x}}_k + \mathbf{B}_k u_k , \quad (2.17)$$

where recall from Equation 2.6 that $u_k = a_k$, the acceleration of the system. The hat notation $\hat{\mathbf{x}}$ indicates the obtained quantity is an estimate and the super index indicates a quantity obtained before the measurement process. This is termed the *a priori* or *time update* stage of the filter, where the system states are estimated without consideration of the measurements. The second step is to incorporate the measurements into the *measurement update* or *a posteriori* state estimation updating the covariance to

$$\mathbf{P}_{k+1} = [(\mathbf{P}_{k+1}^-)^{-1} + \mathbf{H}_{k+1}^T \mathbf{R}_{k+1}^{-1} \mathbf{H}_{k+1}]^{-1} , \quad (2.18)$$

and then the state estimates to

$$\hat{\mathbf{x}}_{k+1} = \hat{\mathbf{x}}_k^- + \mathbf{P}_{k+1} \mathbf{H}_{k+1}^T \mathbf{R}_{k+1}^{-1} (z_{k+1} - \mathbf{H}_{k+1} \hat{\mathbf{x}}_{k+1}^-) = \hat{\mathbf{x}}_k^- + \mathbf{K}_{k+1} (z_{k+1} - \mathbf{H}_{k+1} \hat{\mathbf{x}}_{k+1}^-) , \quad (2.19)$$

where the matrix \mathbf{K} is known as the Kalman gain. In this final form it's easiest to understand the behavior of the filter. The Kalman gain weights the adjustment to the a priori estimate $\hat{\mathbf{x}}_k^-$ once a measurement of the system states z_k is available by modulating the correction to be applied due to the measurement residual, $z_{k+1} - \mathbf{H}_{k+1} \hat{\mathbf{x}}_{k+1}^-$, which is the difference between the a priori state estimate and the actual measurement. In turn, the Kalman gain \mathbf{K} depends on both the covariance matrix \mathbf{Q} of the accelerations affecting the system and the covariance \mathbf{R} of the measurements. Thus, the noise characteristics of both information sources is considered in the estimation process. Equations 2.16-2.19 define what is traditionally called a Kalman filter.

In the above formulation, also referred to as the *forward* filter, the accelerometer time series at sampling interval τ_a provides what is oft referred to as the *system input*, u_k , while the GPS displacements at sampling interval τ_d feed the measurement process, z_k . GPS sampling frequencies are traditionally lower (1 - 10 Hz) than strong-motion accelerometer sampling frequencies (80 - 250 Hz), thus the formulation needs to be adapted to this multi-rate environment (*Smyth and Wu, 2007*) by performing the time update stage (Equations 2.16-2.17) at every time step and applying the measurement update stage (Equations 2.18-2.19) only when a GPS sample becomes available. This is equivalent to having a Kalman gain of zero in the absence of measurements. For algorithmic simplicity it is useful if the sampling frequency of the strong-motion accelerometer is a multiple of GPS sampling frequency. In this way the measurement update can be done at regular intervals but this is not a requirement. Also if the sampling frequencies remain constant throughout and the noise characteristics do not change then \mathbf{A}^s , \mathbf{B}^s , \mathbf{Q}^s , and \mathbf{R}^s remain unchanged. However, the sampling frequencies for both instruments can vary throughout the filtering process as long as the corresponding matrices are modified accordingly. An attractive feature of this formulation is that the matrices involved are dimensionally small making the numerical computation in the two stages of the process simple. Additionally, the Kalman filter only requires knowledge of the current sample and thus can be implemented in real time and across large networks. It must be noted that the Kalman filter will also produce estimates of velocity in conjunction with the displacement computations. A summary of the filter equations can be found in Table 2.1

2.3.2 Optimal Smoothing

Applying the Kalman filter in the forward direction solves what is known as the prediction problem, if data are available over some interval and all that data past and future are used in the estimation then the estimate at any given point can be improved. This is known as the smoothing problem and is a non-real-time or batch operation. It can be performed, nonetheless, as a near real-time operation by limiting the smoothing to short intervals of time. If smoothing happens only

Table 2.1: A summary of Kalman filtering and smoothing equations

Forward Filter	
Initialize states	$\hat{\mathbf{x}}_0 = \mathbf{0}$
Initialize covariance	$\mathbf{P}_0 = \mathbf{I}$
Time update covariance	$\mathbf{P}_{k+1}^- = \mathbf{A}_k \mathbf{P}_k \mathbf{A}_k^T + \mathbf{Q}_k$
Time update system states	$\hat{\mathbf{x}}_{k+1}^- = \mathbf{A}_k \hat{\mathbf{x}}_k + \mathbf{B}_k a_k$
Introduce measurement	$z_k = d_k$
Compute Kalman gain	$\mathbf{K}_{k+1} = \mathbf{P}_{k+1}^- \mathbf{H}_{k+1}^T \mathbf{R}_{k+1}^{-1}$
Measurement update of covariance	$\mathbf{P}_{k+1} = [(\mathbf{P}_{k+1}^-)^{-1} + \mathbf{H}_{k+1}^T \mathbf{R}_{k+1}^{-1} \mathbf{H}_{k+1}]^{-1}$
Measurement update system states	$\hat{\mathbf{x}}_{k+1} = \hat{\mathbf{x}}_{k+1}^- + \mathbf{K}_{k+1} (z_{k+1} - \mathbf{H}_{k+1} \hat{\mathbf{x}}_{k+1}^-)$
RTS N-sample Smoother	
Initialize states	$\mathbf{x}_N = \mathbf{x}_k$
Initialize covariance	$\mathbf{P}_N = \mathbf{P}_k^f$
Compute smoother gain	$\mathbf{F}_k = \mathbf{P}_k^f \mathbf{A}_k (\mathbf{P}_{k+1}^{f-})^{-1}$
Update covariance	$\mathbf{P}_k = \mathbf{P}_k^f - \mathbf{F}_k (\mathbf{P}_{k+1}^{f-} - \mathbf{P}_{k+1}) \mathbf{F}_k^T$
Update system states	$\hat{\mathbf{x}}_k = \hat{\mathbf{x}}_k^f + \mathbf{F}_k (\hat{\mathbf{x}}_{k+1} - \hat{\mathbf{x}}_{k+1}^{f-})$

over a fixed window behind the real-time stream the smoother is called a fixed interval smoother. Any smoother consists of three conceptual steps: the forward Kalman filter described in the previous section, then a backward filter known as the information filter which is applied in reverse time order to the smoothing interval. The third step combines information from the first two steps (forward Kalman filter and information filter) and combines them to generate state estimates. *Rauch et al.* (1965) showed that the forward Kalman and information filters could be applied in a single step. This has come to be known to as the Rauch, Tung and Striebel smoother (RTS). The smoother gain, which is analogous to the Kalman gain, defines the amount of smoothing can be defined

$$\mathbf{F}_k = \mathbf{P}_k^f \mathbf{A}_k (\mathbf{P}_{k+1}^{f-})^{-1} , \quad (2.20)$$

where \mathbf{P}_k^f and \mathbf{P}_{k+1}^{f-} are the a priori and a posteriori covariance matrices, respectively, from the forward filter. The smoothed covariances are given by

$$\mathbf{P}_k = \mathbf{P}_k^f - \mathbf{F}_k (\mathbf{P}_{k+1}^{f-} - \mathbf{P}_{k+1}) \mathbf{F}_k^T , \quad (2.21)$$

and the smoothed state estimates by

$$\hat{\mathbf{x}}_k = \hat{\mathbf{x}}_k^f + \mathbf{F}_k (\hat{\mathbf{x}}_{k+1} - \hat{\mathbf{x}}_{k+1}^{f-}) . \quad (2.22)$$

Note that the smoothing stage works backwards in time using the $k+1$ -th time step to estimate the k -th step and it does not depend on the measurements or system inputs. The RTS smoother consists of applying the forward filter first, and then smoothing using Equations 2.20-2.22. The RTS algorithm requires the totality of the Kalman filtered time series over the smoothing interval to be available as well as all the a priori estimates, covariances, and a posteriori covariances making it a very data intensive operation. For a particular waveform the best possible results are obtained by applying the smoother over the entire duration of the data. For near-real-time computation one can apply the RTS algorithm to segments of data by lagging N samples behind the end of the real time stream. In this fashion it is assumed that the N samples behind the real-time stream constitute a complete time series and the RTS smoother is applied to them. Initialization is performed by setting the N -th sample to $\mathbf{x}_N = \mathbf{x}_k$ and $\mathbf{P}_N = \mathbf{P}_k^f$. Further on we shall show that the important parameter in near-real-time smoothing with this scheme is the number of GPS samples over which one can smooth rather than the actual time lag. A summary of the smoother equations can be found in Table 2.1.

2.3.3 Accelerometer Biases

A subtle point to be considered in this application-specific formulation of the Kalman filter is that the null baseline of most accelerometers is seldom zero. Often due to small tilts or rotations introduced during installation, variations in site and installation conditions, or simply because of drift in the instrument as it ages the DC level of the instrument will be non-zero. In a post-processing scenario one can subtract the opre-event baseline from the accelerometer recording. For real-time calculation however, this cannot be done, and can have a large effect in the Kalman filter output because it introduces a constant acceleration. It can be easily deal with by incorporating the accelerometer bias as an additional system state. If the measured or observed acceleration a^{obs} is related to the true acceleration, a^{true} by

$$a_k^{true} = a_k^{obs} - \Omega_k + \epsilon_a , \quad (2.23)$$

where Ω_k is the DC offset at epoch k and ϵ_a is as before the accelerometer noise. If we augment the system states to include the DC offset we can once again write the continuous difference equation for this system:

$$\frac{d}{dt} \begin{pmatrix} d(t) \\ v(t) \\ \Omega(t) \end{pmatrix} = \frac{d}{dt} \mathbf{x}(t) = \mathbf{A}(t) \mathbf{x}(t) + \mathbf{B}(t) u(t) + \epsilon(t), \quad (2.24)$$

where

$$\mathbf{A} = \begin{pmatrix} 0 & 1 & 0 \\ 0 & 0 & -1 \\ 0 & 0 & 0 \end{pmatrix}; \quad \mathbf{B} = \begin{pmatrix} 0 \\ 1 \\ 0 \end{pmatrix}; \quad u = a^{obs}; \quad \epsilon = \begin{pmatrix} 0 \\ \epsilon_a \\ \epsilon_\Omega \end{pmatrix}, \quad (2.25)$$

where ϵ_Ω is the DC offset noise. A small value of ϵ_Ω will allow the DC offset to vary slowly through time. This means that the noise vector ϵ is Gaussian, such that $\epsilon \sim (0, \mathbf{Q})$ where the covariance \mathbf{Q} depends on the accelerometer and DC offset noise variances σ_a and σ_Ω like

$$\mathbf{Q} = \begin{pmatrix} 0 & 0 & 0 \\ 0 & \sigma_a & 0 \\ 0 & 0 & \sigma_\Omega \end{pmatrix} \quad (2.26)$$

You can again expand the last two equations to verify the system:

$$\frac{d}{dt} \begin{pmatrix} d(t) \\ v(t) \\ \Omega(t) \end{pmatrix} = \begin{pmatrix} \dot{d} \\ \dot{v} \\ \dot{\Omega} \end{pmatrix} = \begin{pmatrix} v \\ -\Omega + a^{obs} + \epsilon_a \\ \epsilon_\Omega \end{pmatrix}. \quad (2.27)$$

We can discretize the continuous system at the sampling rate τ_a of the accelerometer following the strategy outlined in Section 2.3.1

$$\mathbf{A}^s = \mathbf{I} + \mathbf{A}\tau_a + \frac{\mathbf{A}^2\tau_a^2}{2} = \begin{pmatrix} 1 & \tau_a & -\tau_a^2/2 \\ 0 & 1 & -\tau_a \\ 0 & 0 & 1 \end{pmatrix}; \quad (2.28)$$

$$\mathbf{B}^s = \mathbf{B}\tau_a + \frac{\mathbf{A}\mathbf{B}\tau_a^2}{2} = \begin{pmatrix} \tau_a^2/2 \\ \tau_a \\ 0 \end{pmatrix}; \quad (2.29)$$

$$\mathbf{Q}^s = \mathbf{Q}\tau_a + \frac{1}{2}(\mathbf{A}\mathbf{Q} + \mathbf{Q}\mathbf{A}^T)\tau_a^2 + \frac{1}{3}\mathbf{A}\mathbf{Q}\mathbf{A}^T\tau_a^3 = \begin{pmatrix} \sigma_a\tau_a^3/3 & \sigma_a\tau_a^2/2 & 0 \\ \sigma_a\tau_a^2/2 & \sigma_a\tau_a + \sigma_\Omega\tau_a^3/3 & -\sigma_\Omega\tau_a^2/2 \\ 0 & -\sigma_\Omega\tau_a^2/2 & \sigma_\Omega\tau_a \end{pmatrix}. \quad (2.30)$$

Equations 2.28-2.30 can then be used with the standard Kalman filter definition (Table 2.1), except that the output of the filter will now be estimated displacement, velocity and accelerometer bias at each epoch.

2.4 Proof of Concept

Following are examples from shaketable tests of collocated GPS and accelerometers as well as recordings at collocated stations during recent earthquakes to demonstrate the behavior of the Kalman filter

2.4.1 Outdoor shake table testing

A series of earthquake simulations were conducted in 2006-2007 on a full-scale seven-story reinforced concrete wall building at the George E. Brown, Jr. Network for Earthquake Engineering Simulation (NEES) Large High-Performance Outdoor Shake Table (LHPOST) at University of California San Diego (*Panagiotou, 2008; Moaveni et al., 2010*). The four simulations allowed us to test the Kalman filter algorithms in a controlled environment. The LHPOST includes a steel table platform (platen), a reinforced concrete reaction mass, two servo-controlled dynamic actuators with large servo-valves, a platen sliding system with hydrostatic pressure balance bearings, and a real time multi-variable MTS 469DU digital controller with an output of 1024 Hz in displacement. The system is uniaxial and oriented East-West. It can achieve maximum peak-to-peak displacement of ± 0.75 m, velocity of ± 1.8 m/s, and acceleration of ± 3 g, with a frequency bandwidth of 0-20 Hz.

The building with a total height of 19.2 m and total weight of 250 tons was constructed on the shake table platen and subjected to four low to high intensity ground motions, as recorded by accelerometers during the 1971 Mw 6.6 San Fer-

nando and 1994 Mw 6.7 Northridge earthquakes (2.4). The lowest intensity input motion (EQ1) consisted of the longitudinal component from the VNUY station recorded during the San Fernando earthquake. The two medium intensity input motions were the transverse component recorded at the VNUY station obtained during the San Fernando earthquake (EQ2) and the longitudinal component from the WHOX station recorded during the Northridge earthquake (EQ3). The large intensity input motion corresponded to the near-fault Sylmar Olive View Med 360 record during the Northridge earthquake (EQ4), which induced significant nonlinear response. This last class of earthquake is expected to have a 10% probability of exceedance every 50 years. For calibration purposes, the earthquake records were preceded by a sinusoidal signal with peak-to-peak amplitude of about 0.15 m.

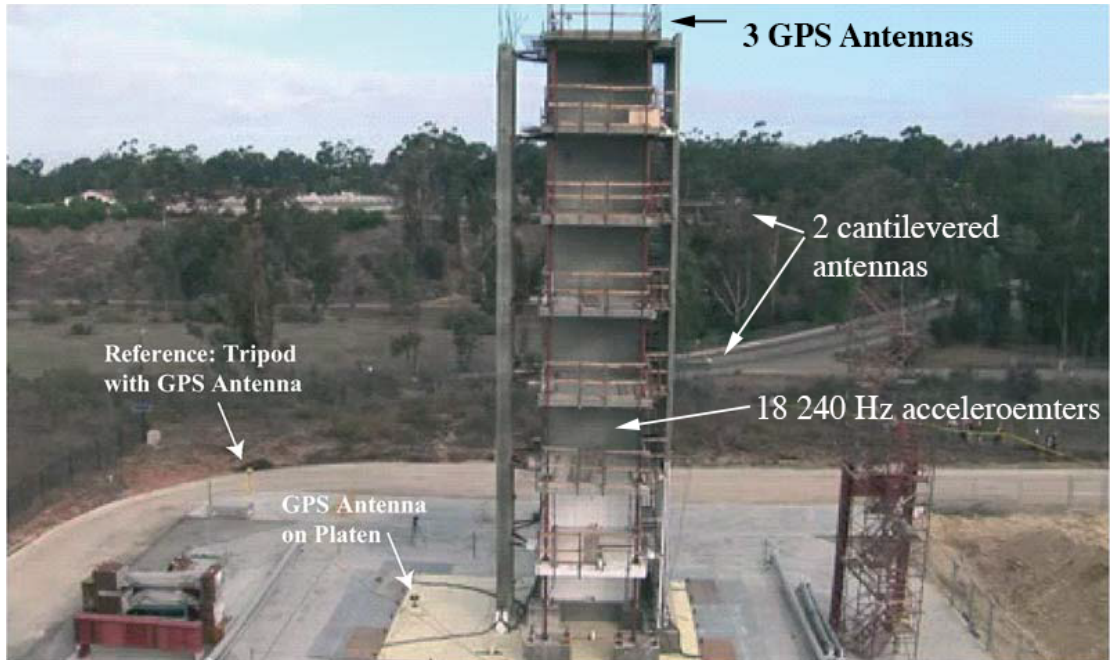


Figure 2.4: Experimental configuration for the 2006 shake table test

The building was instrumented with seven geodetic-quality Navcom NCT-200D GPS receivers sampling at 50 Hz and MEMS-Piezoresistive MSI model 3140 accelerometers sampling at 240 Hz. Three GPS receivers were mounted on the roof (7th floor near the north, south and east corners), and two receivers were cantilevered on the 3rd and 5th floors of the flange wall (east side). A 6th receiver was

located just off the shake table's platen as a stable reference point for measuring displacements. A 7th GPS receiver was situated on the platen. The 15 accelerometers were mounted as follows: 2 on the platen, 4 on the building foundation, 3 on the first floor, 3 on the fifth floor and 3 on the seventh floor (roof). Unfortunately, the north receiver on the roof of the building was not operational during EQ4 due to a loose antenna cable.

GPS phase and pseudorange data were streamed to a PC workstation and 50 Hz displacement waveforms were estimated on-the-fly using the method of instantaneous positioning (*Bock et al.* (2000), see Section 2.2). The "GPS-only" displacements are relative to the fixed coordinates of the GPS receiver just off the platen, which were pre-determined with respect to the true-of-date ITRF2005 coordinates of Plate Boundary Observatory (PBO) station P472 at Camp Elliot (32.8892N, 117.1047W), approximately 656 m away. The accelerometer data were doubly-integrated by high-pass filtering to determine "accelerometer-only" displacements. We re-sampled the 240 Hz raw accelerometer data to 250 Hz to be able to align the times of every 5th point with the 50 Hz Navcom GPS data. Displacement waveforms were then computed using both the forward and the smoothed Kalman (RTS) filter using the GPS platen data as input and, in turn, the raw data from the two platen and four foundation accelerometers. To assess accuracy, we compared the GPS-only, accelerometer-only, and Kalman filter displacements to the input "ground truth" displacements provided at 1024 Hz by the MTS digital controller. To assess precision, we compared the root-mean-square (RMS) of the distances between pairs of accelerometers and pairs of GPS receivers on the roof of the building (7th floor). The results of these comparisons are given in Table 2.2.

Table 2.2: RMS differences between computed displacement waveforms and the input registered by the shake table’s MTS recorder for four earthquake simulations (EQ1-EQ4). We show the results of high pass filtered accelerometer derived displacements for platen accelerometers (PA1 and PA2) and building foundation accelerometers (FA1-4) as well as Kalman filtered waveforms obtained from the platen GPS and platen and foundation accelerometers. We also show the results from decimated data (5 Hz for GPS and 100 Hz for accelerometers, and 1 Hz for GPS and 100Hz for accelerometers). The peak displacements are 0.16-0.17 m for EQ1-EQ3 and 0.40 m for EQ4

Sensors	EQ1	EQ2	EQ3	EQ4
GPS Displacements RMS (m)				
Platen GPS	0.0026	0.0040	0.0029	0.0037
Accelerometer Derived Displacements RMS (m)				
PA1	0.0193	0.0181	0.0151	0.0120
PA2	0.0177	0.0184	0.0131	0.0175
FA1	0.0308	0.0278	0.0037	0.0027
FA2	0.0304	0.0274	0.0036	0.0028
FA3	0.0307	0.0276	0.0037	0.0027
FA4	0.0307	0.0276	0.0036	0.0027
Forward Filter RMS (m)				
PA1+GPS	0.0021	0.0041	0.0034	0.0033
PA2+GPS	0.0021	0.0041	0.0034	0.0033
FA1+GPS	0.0016	0.0021	0.0020	0.0020
FA2+GPS	0.0016	0.0020	0.0020	0.0020
FA3+GPS	0.0016	0.0021	0.0020	0.0020
FA4+GPS	0.0016	0.0021	0.0020	0.0020

Forward Filter + 5 Hz Decimation RMS (m)				
PA1+GPS	0.0041	0.0074	0.0074	0.0046
PA2+GPS	0.0040	0.0074	0.0074	0.0046
FA1+GPS	0.0042	0.0067	0.0063	0.0037
FA2+GPS	0.0042	0.0066	0.0063	0.0037
FA3+GPS	0.0042	0.0066	0.0063	0.0037
FA4+GPS	0.0042	0.0066	0.0063	0.0037
Forward Filter + 1 Hz Decimation RMS (m)				
PA1+GPS	0.0353	0.0211	0.0625	0.0341
PA2+GPS	0.0353	0.0211	0.0625	0.0341
FA1+GPS	0.0333	0.0313	0.0612	0.0273
FA2+GPS	0.0333	0.0305	0.0607	0.0265
FA3+GPS	0.0333	0.0308	0.0609	0.0275
FA4+GPS	0.0333	0.0309	0.0601	0.0277
Forward Filter + RTS Smoothing RMS (m)				
PA1+GPS	0.0016	0.0036	0.0024	0.0028
PA2+GPS	0.0016	0.0036	0.0024	0.0028
FA1+GPS	0.0017	0.0021	0.0021	0.0025
FA2+GPS	0.0017	0.0021	0.0021	0.0025
FA3+GPS	0.0017	0.0021	0.0021	0.0025
FA4+GPS	0.0017	0.0021	0.0021	0.0025
Forward Filter + RTS Smoothing + 5 Hz Decimation RMS (m)				
PA1+GPS	0.0015	0.0038	0.0027	0.0028
PA2+GPS	0.0015	0.0038	0.0027	0.0028
FA1+GPS	0.0017	0.0022	0.0024	0.0025
FA2+GPS	0.0017	0.0022	0.0024	0.0025
FA3+GPS	0.0017	0.0022	0.0024	0.0025
FA4+GPS	0.0017	0.0022	0.0024	0.0025
Forward Filter + RTS Smoothing + 1 Hz Decimation RMS (m)				
PA1+GPS	0.0077	0.0102	0.0152	0.0130

PA2+GPS	0.0077	0.0102	0.0152	0.0130
FA1+GPS	0.0097	0.0117	0.0168	0.0115
FA2+GPS	0.0097	0.0118	0.0166	0.0115
FA3+GPS	0.0098	0.0117	0.0167	0.0114
FA4+GPS	0.0096	0.0117	0.0167	0.0115
Roof Baselines RMS (m)				
GPS (N-S)	0.0033	0.0026	0.0035	n/a
GPS (N-E)	0.003	0.0019	0.0034	n/a
GPS (S-E)	0.0036	0.0033	0.0023	0.0031
Accelerometer (N-S)	0.0008	0.0007	0.001	0.0012

Accuracy of the Displacement Waveforms

Accuracy was determined by comparing the various displacement waveforms with the “truth” displacements provided by the MTS recorder, for each of the four experiments, using the RMS difference as the statistical measure. The results are given in Figure 2.5 and Table 2.2. The peak-to-peak displacements are on the order of 0.17 m for EQ1-EQ3, and 0.4 m for the high intensity Northridge event (EQ4). The RMS statistic is computed over the entire record including dynamic and static periods. The displacements for the single GPS on the platen have an RMS difference of 2.6-4.0 mm, while the displacements for the two accelerometers on the platen have an RMS difference of 12.0-19.3 mm. The larger differences for the accelerometer-derived displacements result from mismatches in amplitude and phase compared to the MTS displacements. The forward Kalman filter solutions reduce the RMS differences by about 10% (except for EQ2 where there is a 10% increase) compared to the GPS-only solutions (2.2-4.1 mm), and there is an additional 10% improvement for all four experiments with the smoothed Kalman filter solutions (1.6-2.3 mm). For the foundation accelerometers, the RMS differences are higher for EQ1 and EQ2 (about 30 mm), but unexpectedly an order of magnitude less for EQ3 and EQ4. In any case, we can conclude that the combined GPS and accelerometer displacement waveforms provide overall mm-level accuracy over the entire range of sampled frequencies, and improved accuracy when compared

to GPS-only or accelerometer-only solutions. The improvement is generally more pronounced when compared to the accelerometer-only solutions. This is not surprising because of the inherent limitations and biases encountered in the double integration of accelerometer data. It is interesting to note that the RMS statistics for either the static or dynamic periods did not differ significantly from the RMS values computed for the entire period (static and dynamic) for any of the experiments. We saw only insignificant degradation (10%) in accuracy during periods of strong shaking.

We repeated the previous analysis with two decimation schemes: the first one decimating the accelerometer to 100 Hz and the GPS to 5 Hz and the second one decimating the accelerometer to 100 Hz and the GPS to 1 Hz (Table 2.2). The latter corresponds to the sampling rates of real-time GPS and strong motion sensors in southern California during the 2010 Mw 7.2 El Mayor-Cucapah earthquake. We find that the fit of the Kalman filtered waveforms is only mildly degraded in the first decimation scheme, and significantly degraded with the second decimation scheme. However smoothing provides a significant improvement, especially at the lower GPS sampling rates (1 Hz). This is an important practical consideration since GPS data are considerably more verbose than strong motion data.

2.5 Application to the M9 Tohoku-oki Earthquake

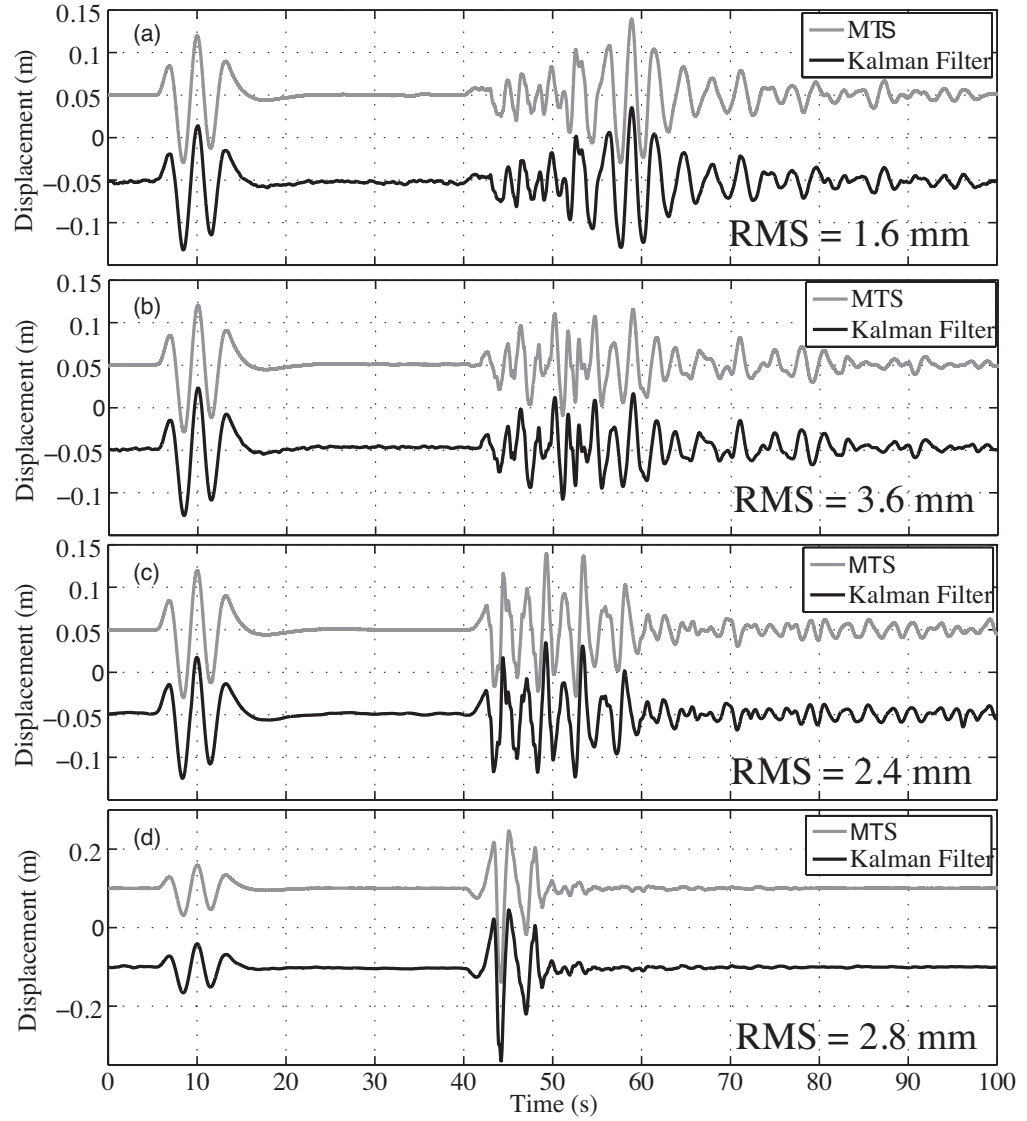


Figure 2.5: Accuracy of broadband displacement waveforms. Root-mean-square (RMS) of the differences between the smoothed Kalman filter displacement waveforms estimated for the four earthquake simulations and the deterministic input as registered at 1024 Hz by the shake table's MTS digital recorder (see also Table 2.2). The waveforms are estimated from the platen GPS and one of the accelerometers on the platen. Note that the vertical scale is the same for (a) through (c) but changes for (d). The two waveforms in each graph have been offset for clarity.

Chapter 3

Rapid Static Modeling

This is only a test.

3.1 A section

Lorem ipsum

Chapter 4

Kinematic Source Inversions

This is only a test.

4.1 A section

Lorem ipsum

Chapter 5

Offshore Data and Tsunami Modeling

This is only a test.

5.1 A section

Lorem ipsum

Chapter 6

Conclusions and Future Outlook

This is only a test.

6.1 A section

Lorem ipsum

Bibliography

- Blewitt, G. (1989). Carrier phase ambiguity resolution for the global positioning system applied to geodetic baselines up to 2000 kilometers. *Journal of Geophysical Research*, 94:10187–10203.
- Bock, Y., Nikolaidis, R. M., Jonge, P. J., and Bevis, M. (2000). Instantaneous geodetic positioning at medium distances with the global positioning system. *Journal of Geophysical Research: Solid Earth (1978–2012)*, 105(B12):28223–28253.
- Bock, Y., Prawirodirdjo, L., and Melbourne, T. (2004). Detection of arbitrarily large dynamic ground motions with a dense high-rate gps network. *Geophysical Research Letters*, 31.
- Boore, D. M. (1999). Effect of baseline corrections on response spectra for two recordings of the 1999 chi-chi, taiwan, earthquake. *U.S. Geol. Surv. Open-File Rept.*, 99(545):1–37.
- Boore, D. M. (2001). Effect of baseline corrections on displacements and response spectra for several recordings of the 1999 chi-chi, taiwan, earthquake. *Bulletin of the Seismological Society of America*, 91(5):1199–1211.
- Boore, D. M. and Bommer, J. J. (2005). Processing of strong-motion accelerograms: needs, options and consequences. *Soil Dynamics and Earthquake Engineering*, 25(2):93–115.
- Boore, D. M., Stephens, C. D., and Joyner, W. B. (2002). Comments on baseline correction of digital strong-motion data: Examples from the 1999 hector mine, california, earthquake. *Bulletin of the Seismological Society of America*, 92(4):1543–1560.
- Chao, W.-A., Wu, Y.-M., and Zhao, L. (2010). An automatic scheme for baseline correction of strong-motion records in coseismic deformation determination. *Journal of seismology*, 14(3):495–504.
- Crowell, B. W., Bock, Y., and Squibb, M. (2009). Demonstration of earthquake early warning using total displacement waveforms from real time gps networks. *Seismological Research Letters*, 80:772–782.

- Dong, D. and Bock, Y. (1989). Global positioning system network analysis with phase ambiguity resolution applied to crustal deformation studies in california. *Journal of Geophysical Research*, 94:3949–3966.
- Emore, G. L., Haase, J. S., Choi, K., Larson, K. M., and Yamagiwa, A. (2007). Recovering seismic displacements through combined use of 1-hz gps and strong-motion accelerometers. *Bulletin of the Seismological Society of America*, 97(2):357–378.
- Geng, J. (2010). *Rapid integer ambiguity resolution in GPS precise point positioning*. PhD thesis, University of Nottingham, Nottingham, UK.
- Geng, J., Bock, Y., Melgar, D., Crowell, B. W., and Haase, J. S. (2013a). A new seismogeodetic approach applied to gps and accelerometer observations of the 2012 brawley seismic swarm: Implications for earthquake early warning. *Geochemistry, Geophysics, Geosystems*.
- Geng, J., Melgar, D., Bock, Y., Pantoli, E., and Restrepo, J. (2013b). Recovering coseismic point ground tilts from collocated highrate gps and accelerometers. *Geophysical Research Letters*, 40(19):5095–5100.
- Genrich, J. F. and Bock, Y. (2006). Instantaneous geodetic positioning with 10–50 hz gps measurements: Noise characteristics and implications for monitoring networks. *Journal of Geophysical Research: Solid Earth (1978–2012)*, 111(B3).
- Graizer, V. M. (1979). Determination of the true ground displacement by using strong motion records. *Izvestiya Academy of Sciences, USSR, Physics of the Solid Earth*, 15(12):875–885.
- Graizer, V. M. (2006). Tilts in strong ground motion. *Bulletin of the Seismological Society of America*, 96(6):2090–2102.
- Havskov, J. and Alguacil, G. (2006). *Instrumentation in Earthquake Seismology*. Springer, New York, NY, first edition.
- Iwan, W. D., Moser, M. A., and Peng, C.-Y. (1985). Some observations on strong-motion earthquake measurement using a digital accelerograph. *Bulletin of the Seismological Society of America*, 75(5):1225–1246.
- Kalman, R. E. (1960). A new approach to linear filtering and prediction problems. *Journal of basic Engineering*, 82(1):35–45.
- Larson, K. M., Bodin, P., and Gomberg, J. (2003). Using 1-hz gps data to measure deformations caused by the denali fault earthquake. *Science*, 300(5624):1421–1424.

- Lewis, F. L., Xie, L., and Popa, D. (2008). *Optimal and robust estimation: with an introduction to stochastic control theory*, volume 26. CRC.
- Miyazaki, S., Larson, K. M., Choi, K., Hikima, K., Koketsu, K., Bodin, P., Haase, J., Emore, G., and Yamagiwa, A. (2004). Modeling the rupture process of the 2003 september 25 tokachi-oki (hokkaido) earthquake using 1-hz gps data. *Geophysical Research Letters*, 31(L21603).
- Moaveni, B., He, X., Conte, J. P., Restrepo, J. I., and Panagiotou, M. (2010). System identification study of a 7-story full-scale building slice tested on the ucsd-nees shake table. *Journal of Structural Engineering*, 137(6):705–717.
- Nikolaidis, R. M., Bock, Y., Jonge, P. J., Shearer, P., Agnew, D. C., and Van Domselaar, M. (2001). Seismic wave observations with the global positioning system. *Journal of Geophysical Research: Solid Earth (1978–2012)*, 106(B10):21897–21916.
- Panagiotou, M. (2008). *Seismic design, testing and analysis of reinforced concrete wall buildings*, volume PhD Thesis. University of California San Diego.
- Pillet, R. and Virieux, J. (2007). The effects of seismic rotations on inertial sensors. *Geophysical Journal International*, 171(3):1314–1323.
- Rauch, H. E., Striebel, C., and Tung, F. (1965). Maximum likelihood estimates of linear dynamic systems. *AIAA journal*, 3(8):1445–1450.
- Smalley, R. (2009). High-rate gps: How high do we need to go? *Seismological Research Letters*, 80(6):1054–1061.
- Smyth, A. and Wu, M. (2007). Multi-rate kalman filtering for the data fusion of displacement and acceleration response measurements in dynamic system monitoring. *Mechanical Systems and Signal Processing*, 21(2):706–723.
- Trifunac, M. D. and Todorovska, M. I. (2001). A note on the useable dynamic range of accelerographs recording translation. *Soil Dynamics and Earthquake Engineering*, 21(4):275 – 286.
- Tsuda, K., Steidl, J., Archuleta, R., and Assimaki, D. (2006). Site-response estimation for the 2003 miyagi-oki earthquake sequence considering nonlinear site response. *Bulletin of the Seismological Society of America*, 96(4A):1474–1482.
- Tu, R., Wang, R., Zhang, Y., and Walter, T. R. (2014). Application of a net-based baseline correction scheme to strong-motion records of the 2011 mw 9.0 tohoku earthquake. *Geophysical Journal International*, page ggu092.
- Wang, R., Parolai, S., Ge, M., Jin, M., Walter, T. R., and Zschau, J. (2013). The 2011 mw 9.0 tohoku earthquake: Comparison of gps and strong motion data. *Bulletin of the Seismological Society of America*, 103(2B):1336–1347.

- Wang, R., Schurr, B., Milkereit, C., Shao, Z., and Jin, M. (2011). An improved automatic scheme for empirical baseline correction of digital strong-motion records. *Bulletin of the Seismological Society of America*, 101(5):2029–2044.
- Wu, Y.-M. and Wu, C.-F. (2007). Approximate recovery of coseismic deformation from taiwan strong-motion records. *Journal of seismology*, 11(2):159–170.
- Zumberge, J. F., Heflin, M. B., Jefferson, D. C., and M, W. M. (1997). Precise point positioning for the efficient and robust analysis of gps data from large networks. *Journal of Geophysical Research*, 102:5005–5017.